# Growth-Driven Polymorphism Engineering and Direct Phase Modulation of α- and β'-In2Se3

**Tianru Wu**

trwu@sjtu.edu.cn

Shanghai Jiao Tong University

**Lei Xu**

Shanghai Jiao Tong University

**Dongyan Liu**

Shanghai Jiao Tong University

**Zhenhua Wu**

Shanghai Jiao Tong University https://orcid.org/0000-0002-5527-0310

**Han Chen**

Shanghai Jiao Tong University

**Yutao Han**

Shanghai Jiao Tong University

**Mingzheng Wang**

Shanghai Jiao Tong University

**Haoyue Guo**

Shanghai Jiao Tong University

**Tian Tan**

Shanghai Jiao Tong University

**Yakui Mu**

Shanghai Jiao Tong University

**Yang Wang**

Shanghai Jiao Tong University

**ZengQin Song**

Shanghai Jiao Tong University

**Qunli Rao**

Shanghai Jiao Tong University

**Xuewei Feng**

Shanghai Jiao Tong University

**Yakun Yuan**

Shanghai Jiao Tong University https://orcid.org/0000-0001-7384-9767

**Lei Shi**

University of Science and Technology of China

**Xiaotian Zhang**

Shanghai Jiao Tong University

**Article**

**Keywords:**

**Posted Date:** August 28th, 2025

**DOI:** https://doi.org/10.21203/rs.3.rs-7385740/v1



**Additional Declarations:** There is **NO** Competing Interest.

# Growth-Driven Polymorphism Engineering and Direct Phase Modulation of α- and β′-$In_2Se_3$

**Lei Xu[1], Dongyan Liu[1], Zhenhua Wu[1], Han Chen[1], Yutao Han[1,2], Mingzheng Wang[2,3], Haoyue Guo[1], Tian Tan[1], Yakui Mu[1], Yang Wang[1], Zengqin Song[1], Qunli Rao[4], Xuewei Feng[1], Yakun Yuan[2,5], Lei Shi[6], Xiaotian Zhang[1*] and Tianru Wu[1*]**

[1]School of Mechanical Engineering, Shanghai Jiao Tong University, Shanghai 200240, P. R. China

[2]Future Material Innovation Center, Zhangjiang Institute for Advanced Study, Shanghai Jiao Tong University, Shanghai, 200240, P. R. China

[3]School of Materials Science and Engineering, Shanghai Jiao Tong University, Shanghai, 200240, P. R. China

[4]Instrumental Analysis Center, Shanghai Jiao Tong University, Shanghai, 200240, P. R. China

[5]School of Physics and Astronomy, Shanghai Jiao Tong University, Shanghai, 200240, P. R. China

[6]Hefei National Research Center for Physical Sciences at the Microscale, University of Science and Technology of China, Hefei, Anhui 230026, P. R. China

* E-mail: xiaotianzhang@sjtu.edu.cn * E-mail: trwu@sjtu.edu.cn

**Abstract**

Two-dimensional (2D) $In_2Se_3$ represents a uniquely versatile platform for novel electronics, hosting the rare coexistence of paraelectric (β), antiferroelectric (β'), and ferroelectric (α) phases. However, synthesizing phase-pure $In_2Se_3$ films, particularly the critical ferroelectric semiconducting α-phase, is fundamentally hindered by the subtle structural distinctions and minimal energetic differences among its polymorphs. Here, we directly reveal phase-selective growth of $In_2Se_3$ on mica using cross-sectional transmission electron microscopy (TEM). It is found that both chemical vapor deposition (CVD) and physical vapor deposition (PVD) techniques yield exclusively either the pure β′ phase or coexisting monolayer α and β′ phases, with the cooling rate

playing a critical role in phase selection. Crucially, in situ stress release within the epitaxial film on mica generates wrinkles propagating along the <1$\bar{1}$00> direction, triggering an immediate β' to α phase transformation. The resulting phase-pure α-$In_2Se_3$ films enable ferroelectric transistors exhibiting a high electron mobility of 259 $cm^2 V^{-1} s^{-1}$. This precise control over polymorph synthesis unlocks promising opportunities for 2D ferroelectric devices and nanoelectronics, offering a pathway to harness phase-specific functionalities.

2D van der Waals (vdW) ferroelectric materials exhibit robust ferroelectricity down to the atomic scale, positioning them as key enablers for ultrahigh-density integration and low-power electronics[1]. Among these, 2D $In_2Se_3$ stands out for its rich polymorphism, offering a versatile platform for novel device concepts through tailored exploitation of its diverse physical properties. Current research primarily focuses on its α, β′, and β phases. The room-temperature-stable α-phase exhibits a non-centrosymmetric structure and robust ferroelectricity even at the monolayer limit, making it a highly promising ferroelectric semiconductor. In contrast, the β′-phase exhibits in-plane ferroelectricity[2], antiferroelectricity[3] , and ferroelasticity[4]. As the parent phase of β′, centrosymmetric β-$In_2Se_3$ displays paraelectric behavior. These distinct phase-dependent tunabilities make it a prime material for ferroelectric field-effect transistors (FET)[5,6], ferroelectric semiconductor junctions (FSJ)[7], neuromorphic computing[8] and optoelectronic detectors[9].

Despite the intriguing polymorphism, subtle structural and energetic distinctions among the α, β, and β′-phases have sparked persistent identification controversies. These distinctions also pose formidable challenges for phase-selective synthesis, particularly in achieving the controlled growth of phase-pure α-$In_2Se_3$. The predominant synthesis routes, such as mica-based chemical vapor deposition (CVD) using Se + $In_2O_3$ precursors and physical vapor deposition (PVD) with $In_2Se_3$ powder, often yield inconsistent phase outcomes. Reported products range from α-phase[7,10-15], β′-$In_2Se_3$[4,16-18] to mixed-phase[16,17,19,20], indicating profound sensitivity to synthetic conditions. For instance, Lin *et al.* associated α-phase formation via CVD with slow

cooling[16,18,21,22], while Si *et al.* achieved it via low-temperature salt-assisted PVD[23]. Notably, distinct deviations could be observed in the Raman spectra of synthesized α-$In_2Se_3$[10,15,16,21,24-26] compared to mechanically exfoliated α-$In_2Se_3$ flakes[27,28], whereas the β and β′ phases even show near-identical signatures[6,27]. This further complicates phase identification in synthesized $In_2Se_3$. Additionally, Zheng et al. reported α-phase formation is confined to the first few layers in PVD-grown films on mica[17], while Han et al. suggest that Se+$In_2O_3$ CVD primarily yields β-$In_2Se_3$, achieving α-$In_2Se_3$ indirectly via transferring β'-$In_2Se_3$ onto the uneven substrate[6]. Although this study demonstrates potential route for large-area α-$In_2Se_3$ fabrication, the fundamental mechanisms underlying strain generation on mica and its subsequent relaxation on uneven substrate remain unresolved. Some recent advances offer other strategies for direct α-phase synthesis[29-31], significant challenges persist for robust and scalable synthesis methods for large-area and phase-pure α-$In_2Se_3$, which is critical for the advancement of 2D ferroelectric devices.

In this work, we employ cross-sectional aberration-corrected scanning transmission electron microscopy (AC-STEM) to systematically elucidate the phase-selective growth of $In_2Se_3$ on mica via both CVD and PVD under varying conditions. In situ heating/cooling X-ray diffraction (XRD) and differential scanning calorimetry (DSC) analyses of α-$In_2Se_3$ reveal the phase transition sequences among the α, β, and β' phases. Crucially, CVD/PVD growth with a slow cooling rate consistently yields a heterostructure comprising a monolayer α-phase beneath the multilayer β′-phase on mica, which we attribute to epitaxial constraints imposed by the mica substrate. Building on this insight, we achieve direct β′→α phase transformation on mica through controlled strain release, which generates wrinkles that propagating along $<1\bar{1}00>$ crystallographic direction. We further demonstrate reversible β′→α→β′ phase transitions via annealing, with in-plane XRD precisely tracking the evolution of interplanar spacing during phase changes. Finally, field-effect transistors fabricated from phase-pure α-$In_2Se_3$, β′-$In_2Se_3$, and vertical α/β′ heterophase junctions exhibit outstanding performance, including high carrier mobility (up to 259 $cm^2 V^{-1} s^{-1}$), large on/off ratios (>$10^7$), and wide memory windows (~136 V).

**Phase-selective growth conditions and mechanism of $In_2Se_3$ on mica substrates.**

To address the ongoing debate regarding phase segregation in vapor-deposited $In_2Se_3$, we systematically compared the synthesis of $In_2Se_3$ films on mica substrates using two distinct methodologies: PVD with α-$In_2Se_3$ powder and CVD employing Se and $In_2O_3$ precursors. By controlling growth time, we can obtain large-area $In_2Se_3$ thin films (Supplementary Fig. 1). Unambiguous phase identification was achieved through comprehensive cross-sectional and plan-view transmission electron microscopy (TEM) analysis. We first investigated the influence of cooling rate on polymorph formation in multilayer $In_2Se_3$ films by employing both slow and rapid cooling protocols. Fig. 1a presents a representative cross-sectional high-angle annular dark-field STEM (HAADF-STEM) image (viewed along the $[11\bar{2}0]$ zone axis) of the CVD-grown $In_2Se_3$ film via rapid cooling. It reveals quintuple layers (QLs) with Se–In–Se–In–Se atomic sequence separated by vdW gaps. The position of the central Se atom definitively excludes the presence of the α-phase.

We further distinguished the as-grown films between the commonly reported high-temperature β-phase and its room-temperature polymorph, β′-$In_2Se_3$[32,33]. Although structurally related, the β′ phase is unambiguously identified by its characteristic modulated nanostriped superstructure, which arises from a distortion of the parent β-phase[2-4]. High-resolution TEM (HRTEM) image (Fig. 1a, top view) of transferred films onto a copper grid reveals periodic stripes oriented along <$11\bar{2}0$> with a characteristic width of $4d_{1\bar{1}00}$. This nanostriped superstructure is further corroborated by satellite diffraction spots in the corresponding selected-area electron diffraction (SAED) pattern (Fig. 1a, inset). The intensity profile across the magnified diffraction pattern (Supplementary Fig. 2a) confirms a <$11\bar{2}0$>-directed periodicity of n/8, corresponding precisely to the $4d_{1\bar{1}00}$ width of the nanostripes. Polarized light optical microscopy further reveals typical domain structures in the as-grown $In_2Se_3$ films (Supplementary Fig. 2b). Rapidly cooled PVD-grown $In_2Se_3$ films also exhibit similar nanostrips and satellite reflections (Fig. 1b). Collectively, these results unambiguously indicate that both CVD and PVD procedure with a rapid cooling rate yield pure β′-$In_2Se_3$.

Subsequently, we examined the impact of slow cooling on phase evolution in both CVD- and PVD-deposited $In_2Se_3$. Cross-sectional TEM images (Figs. 1c, d) reveal the presence of an initial α-$In_2Se_3$ monolayer at the epitaxial film/mica interface for both techniques. Top-view HRTEM combined with SAED analysis definitively identifies the overlying multilayer as β′-phase. Furthermore, HRTEM image (Fig. 2a) reveals a 120° domain wall formed by the reorientation of nanostrip between adjacent domains[4], a structural feature corroborated by SAED patterns exhibiting satellite reflections indicative of bidirectional nanostrip ordering[4].

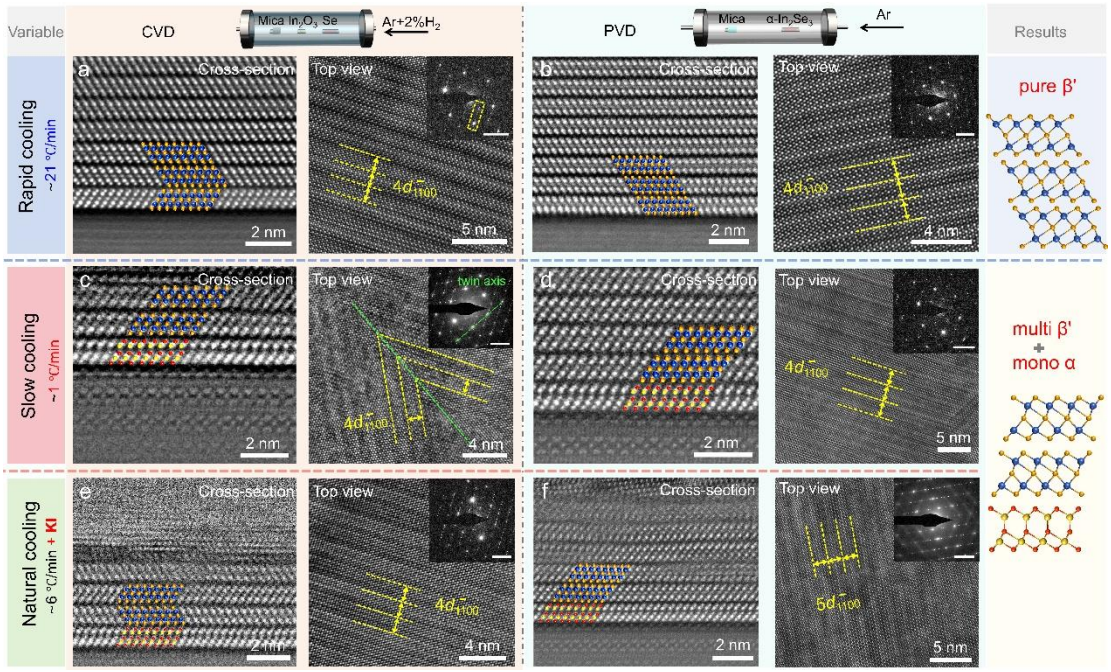


**Figure 1| Phase identification of $In_2Se_3$ films grown on mica substrates via CVD (using Se + $In_2O_3$ precursors) and PVD (using α-$In_2Se_3$ powder) under various growth conditions.** Cross-sectional AC-STEM and top-view HRTEM images of $In_2Se_3$ grown under rapid cooling conditions via **a** CVD and **b** PVD, under slow cooling conditions via **c** CVD and **d** PVD, under natural cooling conditions via e salt-assisted CVD f salt-assisted PVD. Inset: Corresponding SAED patterns. (Scale bar: 5 1/nm).

To explore phase formation at lower temperatures, we also employed salt-assisted vapor deposition under natural cooling conditions (620 °C for CVD, 750 °C for PVD). Remarkably, this approach likewise yielded exclusively heterophase structures consisting of a monolayer α-$In_2Se_3$ coupled with multilayer β'-$In_2Se_3$ (Fig. 1e, f). Plan-view HRTEM (Fig. 1f) revealed adjacent nanostrips with a characteristic width of

$5d_{1\bar{1}00}$. In addition to the two types of nanostripe widths observed in our β'-$In_2Se_3$, Wang et al. also reported antiparallel stripes with $5d_{1\bar{1}00}/4d_{1\bar{1}00}$ configurations[34]. Raman spectra, second-harmonic generation (SHG) and photoluminescence (PL) spectra for films grown under all six conditions are presented in Supplementary Fig. 3-5. The Raman signatures across all samples are perplexingly similar and correspond to literature reports assigned to both β- and α-phases[6,11,19,35]. Additionally, all of these samples exhibit extremely weak SHG and PL responses. These comprehensive analyses lead to two key conclusions: 1. The polymorph evolution of $In_2Se_3$ on mica is fundamentally independent of the specific deposition technique (e.g., precursor variants or salt assistance). 2. Modulation of the cooling rate serves as the dominant factor, exclusively yielding either pure β′-phase films or vertical heterophase structures consisting of multilayer β′-phase on monolayer α-phase. Consequently, the direct growth-driven synthesis of phase-pure α-$In_2Se_3$ films on mica remains an unresolved fundamental challenge.

To elucidate the origin of phase-purity limitations in CVD/PVD-grown α-$In_2Se_3$ on mica, we investigated the α, β and β′ phase transition using in situ heating/cooling XRD (Supplementary Fig. 6a). α-$In_2Se_3$ powder was heated to 400 °C at a rate of 10 °C/min, followed by rapid quenching in liquid nitrogen (50°C/min), while monitoring the evolution of lattice spacing for in-plane $(11\bar{2}0)$ / $(1\bar{1}00)$ and out-of-plane (0006) reflections. As shown in Fig. 2a, pronounced discontinuities in all lattice spacing were observed near 200°C during both heating and cooling process. Above the Curie temperature of α-$In_2Se_3$ (200°C), heating induces a transformation to high temperature β-phase. Rapid quenching to room temperature results in compressed lattice spacings in both in-plane and out-of-plane directions relative to the initial α-phase, indicating an irreversible transition. The quenched $In_2Se_3$ films further exhibits characteristic peak splitting in XRD (Supplementary Fig. 6b), manifesting anisotropic lattice distortion and symmetry breaking inherent to β′-$In_2Se_3$ phase [3]. This α→β→β′ transition sequence was corroborated by DSC (Fig. 2b): an endothermic peak at 212 °C (heating) confirms the α→β transition, while an exothermic peak at 196 °C (cooling) corresponds to β→β′ transition. Notably, the quenched α-$In_2Se_3$ powder transforms into β′-phase, exhibiting significantly greater peak shifting for the $(11\bar{2}0)$ reflection compared to $(1\bar{1}00)$ in XRD

patterns (Supplementary Fig. 7). This indicates that the interplanar spacing of the $(11\bar{2}0)$ plane undergoes more pronounced compression than that of the $(1\bar{1}00)$ planes during the α→β' phase transition.

To further probe the kinetics of phase transformation, we performed powder XRD measurements on residual $In_2Se_3$ precursors after PVD growth under varying cooling rates (Supplementary Fig. 8). The α-phase coexists with β′-phase in all residual precursors, with its fraction inversely proportional to the cooling rate, as quantified by the intensity ratio of α (0006) to β′ (0006) reflections (Fig. 2c). This demonstrates enhanced β′-to-α conversion at slower cooling rates. The inset of Fig. 2c confirms that liquid-nitrogen-quenched material retains pure β′-phase, while slowly cooled precursors achieve near-complete reversion to α-phase. Importantly, both the as-grown film and its precursor source reside within the same PVD thermal zone. After growth, the remnant precursor reverts predominantly to α-phase, whereas the $In_2Se_3$ film on mica stabilizes primarily as the β′-phase (or exhibits β′-$In_2Se_3$ on monolayer α-$In_2Se_3$ ) This stark contrast strongly implicates a substrate-mediated stabilization mechanism. Recent studies highlight the sensitivity of $In_2Se_3$ domain orientation to subtle PVD-growth variations[23], coupled with computational simulations of epitaxial relationships. To elucidate the PVD-specific epitaxy on mica, we therefore employed a combined micro-scale TEM and macro-scale in-plane XRD approach.

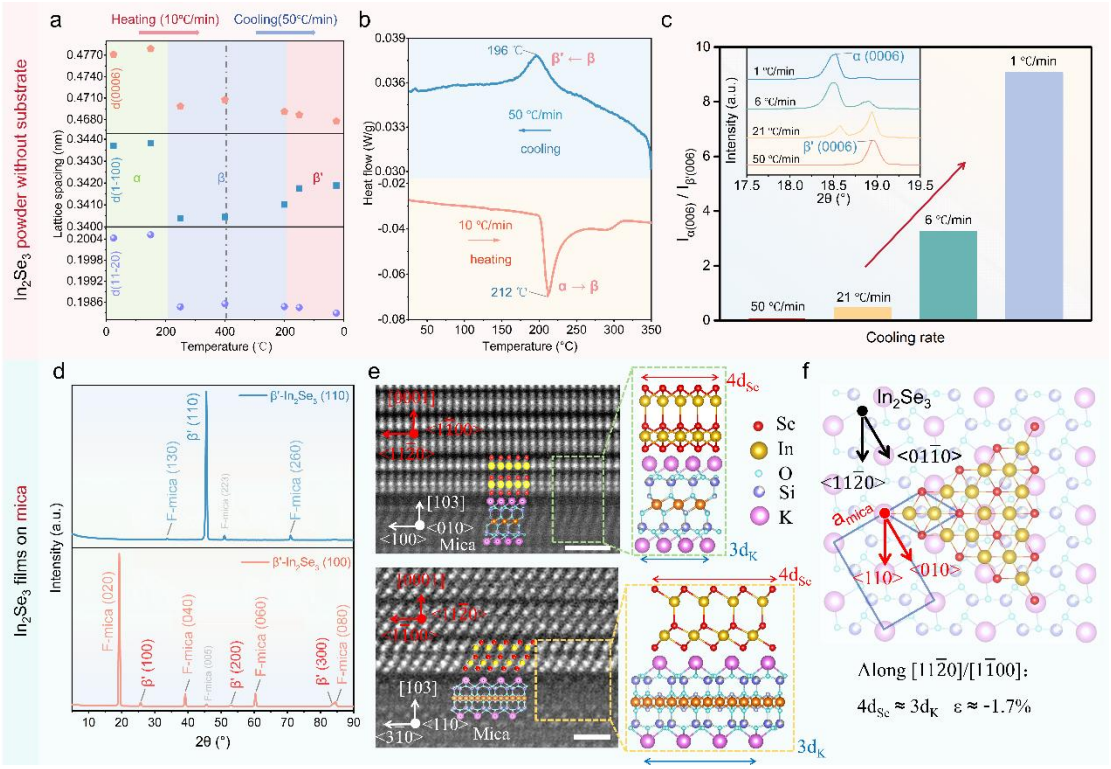


**Figure 2| Growth mechanisms of β′-phase or monolayer α-phase coupled with multilayer β′-phase $In_2Se_3$ on mica substrates via CVD and PVD. a** Out of plane and in-plane lattice spacing of α-$In_2Se_3$ powder as a function of temperature extracted from in situ XRD for both heating and cooling processes. **b** DSC curve reveals temperature for phase transition (α → β → β′) during heating and cooling processes. **c** Comparison of $I_{\alpha(0006)}/I_{\beta'(0006)}$ ratios in $In_2Se_3$ powder obtained at different cooling rates. Inset: Comparison of (006) diffraction peak intensities between α-$In_2Se_3$ and β'-$In_2Se_3$ under varying cooling rates. **d** In-plane XRD θ-2θ diffractograms of (110) $In_2Se_3$/mica (top) and (100) $In_2Se_3$/mica (bottom). **e** Cross-sectional HAADF images of the as-grown $In_2Se_3$/mica interface captured along the <11$\bar{2}$0> and <1$\bar{1}$00> zone axes of $In_2Se_3$. Scale bar: 1 nm **f** Schematic diagram of the 4×4 α-$In_2Se_3$ on $3 \times \sqrt{3}$ F-mica.

In-plane XRD measurements (Fig. 2d) reveal the epitaxial relationships: (11$\bar{2}$0) $In_2Se_3$ ∥ (130) mica and (10$\bar{1}$0) $In_2Se_3$ ∥ (010) mica. This aligns precisely with the cross-sectional AC-STEM observations (Fig. 2e), where the relationship 4dSe ≈ 3dK holds along both the [1$\bar{1}$00] and [11$\bar{2}$0] directions. Consequently, the epitaxial relationship for PVD-grown $In_2Se_3$ on mica can be described by a 4×4 $In_2Se_3$ unit cell matching a 3×√3 mica supercell (Fig. 2f). The resulting lattice mismatch for epitaxial $In_2Se_3$ is

calculated to be -1.7%, imposing compressive strain that kinetically traps the β′-phase by suppressing lattice expansion required for β′→α transition. This explains the inherent α-phase growth limitation on mica. In addition, the stabilization of multilayer β′-$In_2Se_3$/ monolayer α-$In_2Se_3$ achieved by reducing the cooling rate can be attributed to the interfacial strain release to the flexible mica substrate, consistent with previous reports of misfit strain transfer to mica substrate side[36,37]. This mechanism is further corroborated by growth experiments on rigid highly oriented pyrolytic graphite (HOPG). Here, cross-sectional AC-STEM analysis definitively demonstrates the presence of pure β′-$In_2Se_3$ (Detailed in Supplementary Fig.9). Due to the inability of stress to transfer to the rigid HOPG substrate, the first $In_2Se_3$ layer at interface retains the β′ phase rather than transforming into the α phase.

**Direct phase transition (β′→α→β′) of $In_2Se_3$ on mica**

During cooling process after growth, the naturally formed β′-$In_2Se_3$ phase exhibits intrinsically compressed in-plane and out-of-plane lattice spacings relative to the α-phase. These inherent characteristics amplified by compressive epitaxial stress from the mica substrate, collectively impede the direct growth of pure, multilayer α-$In_2Se_3$. Here, we developed a strategy for the direct synthesis of α-$In_2Se_3$ via in situ strain engineering. As illustrated in Fig. 3a, localized mechanical contact was applied directly to the as-grown β′-$In_2Se_3$ film on mica using a metal probe. This process instantly releases compressive stress, triggering lattice expansion in the form of microscale wrinkles and simultaneously driving a complete β′→α phase transformation. Fig. 3b presents optical images of PVD-grown β′-$In_2Se_3$ films on mica before and after strain release. The forming wrinkles preferentially propagate along the <1$\bar{1}$00> crystallographic direction and complete transformation to α-phase occurs within 120 seconds (Supplementary Fig. 10). AFM image (Supplementary Fig. 11) reveals wrinkle heights reaching several hundred nanometers. To demonstrate the robustness and reproducibility of this strategy, in situ strain release was recorded on both PVD- and CVD grown continuous films and triangular β′-$In_2Se_3$ domains (Supplementary Figs. 12-15; Supplementary Videos 1-4).

Cross-sectional AC-STEM analysis of the wrinkle structure (Fig. 3c) reveals delamination at the α-$In_2Se_3$/mica interface (Fig. 3d). This indicates that compressive stress release initiates from the interfacial β′-$In_2Se_3$ layer, enabling the formation of phase-pure multilayer α-$In_2Se_3$. Atomic-resolution image within the wrinkle confirms propagation along <1$\bar{1}$00> and identifies two distinct bending modes: arcs and kinks

(Fig. 3e). Remarkably, the central Se atoms within the α-$In_2Se_3$ QLs remain unchanged across arcs,, whereas antiparallel offsets at kinks sites create adjacent domains with opposing polarization (Fig. 3f). This bending behavior is determined by a critical angle ($\theta_{critical} = 34°$)[38]: arcs form for $\theta < \theta_{critical}$, while kinks emerge at $\theta > \theta_{critical}$. Accordingly, we observe 32° arc bends alongside 47° and 57° kinks at top of the wrinkle. Two additional HAADF images of 44° kinks at bottom of the wrinkle are shown in Supplementary Fig. 16. Furthermore, polarized light optical microscopy captured the real-time disappearance of domain structures as wrinkles propagated, signifying the β′→α transition (Supplementary Fig. 17 and Supplementary Video 5). Thus， this approach successfully achieved centimeter-scale α-$In_2Se_3$ films (Supplementary Fig. 18).

To directly visualize the stress evolution during wrinkle formation, we employed in situ XRD to monitor changes in the in-plane interplanar spacings of the (100) and (110) planes of β′-$In_2Se_3$ on mica before and after stress relaxation. Fig. 3g shows that lattice spacing of mica substrate remains virtually unchanged. In stark contrast, both the (100) and (110) spacings of β′-$In_2Se_3$ increase significantly, with substantially greater expansion observed for the (110) planes. These results unambiguously confirm that β′-$In_2Se_3$ on mica experiences in-plane compressive stress. Upon relaxation, the β′-$In_2Se_3$ lattice expands in-plane and delaminates from the mica substrate. This anisotropic expansion, with the (110) planes exhibiting significantly greater dilation than the (100) planes, drives wrinkle propagation along the <$1\bar{1}00$> direction. Out-of-plane (0006) spacing also expands after stress release (Supplementary Fig. 19).

Importantly, the changes in interplanar spacings during the β′→α transition in stress-released films on mica are identical to those observed during the spontaneous β′→α transition in slowly cooled β′-$In_2Se_3$ powder. Cross-sectional AC-STEM image of the strain-released films on mica (Fig. 3h) validates the synthesis of phase-pure α-$In_2Se_3$. This contrasts with indirect methods requiring β′-$In_2Se_3$ transfer onto uneven substrates for strain manipulation[6]. Crucially, the atomically sharp interface confirms preservation of the original epitaxy: [$11\bar{2}0$] $In_2Se_3$ ∥ [110] mica, consistent with in-plane XRD results. Moreover, plan-view HRTEM of the released α-$In_2Se_3$ reveals pristine lattice fringes devoid of nanostrips, with corresponding SAED patterns exhibiting no satellite spots. Together, these features definitively confirm the crystallographic characteristics of the α-phase.

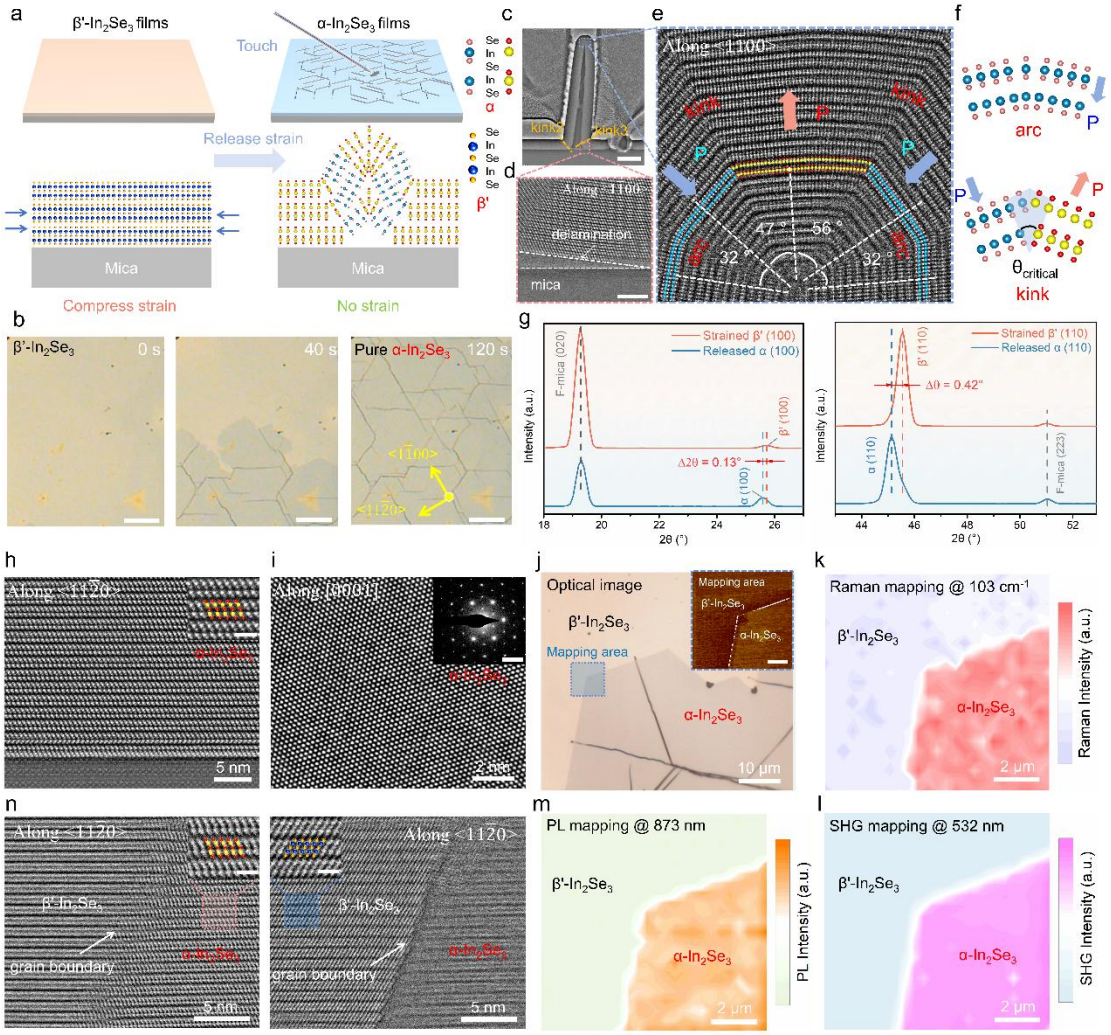


**Figure 3| Direct fabrication of α-$In_2Se_3$ on mica substrates via novel phase engineering. a** Schematic illustration of the β' to α phase transition triggered by wrinkle formation via metal probe contact on β'-$In_2Se_3$ film grown on mica. **b** In situ optical image showing wrinkle propagation in stress-released β'-$In_2Se_3$ film grown on mica. Scale bar: 2 μm **c** Cross-sectional HAADF image of the wrinkle. **d** Magnified HAADF image of delamination at $In_2Se_3$/mica interface. **e** AC-STEM image of two kinks and arcs at the top of wrinkle. **f** Schematic diagram of atomic arrangement for two types of bends within the wrinkle. **g** Comparison of (100) and (110) interplanar spacings in β′-$In_2Se_3$ (strained) versus α-$In_2Se_3$ (strain released) films on mica. **h** Cross-sectional HAADF image of strain released multilayer α-$In_2Se_3$/F-mica interface, recorded along the <11$\bar{2}$0> direction of α-$In_2Se_3$. **i** Top view HRTEM image of strain released α-$In_2Se_3$ films and corresponding SAED pattern. Optical image of the interfacial region between strain-released α-$In_2Se_3$ and as-grown β′-$In_2Se_3$ area. Inset: AFM image of the area

within the dashed rectangle. Scale bar: 2 μm. **k-m** Raman, SHG and PL mapping across the strain-released (α)/strain-retained (β′) area. **n** Cross-sectional HAADF imaging of the α/β′ phase boundary between strain-relaxed and strain-retained regions.

Direct property comparisons between strain-released (α-phase) and strained (β′-phase) regions further validate the transformation. The optical image (Fig. 3j) shows this phase boundary with distinct color modulation. Spatially resolved Raman, SHG, and PL mapping (Fig. 3k-m) across the phase boundary (dashed box, Fig. 3j) reveal a homogeneous α-phase transformation (Raman at 103 $cm^{-1}$), a strong SHG response in non-centrosymmetric α-$In_2Se_3$ (compared to negligible signal in β′), and a direct bandgap of 1.4 eV (PL) in the α-phase (Spectra comparisons shown in Supplementary Fig. 20). All mapping profiles exhibit exact spatial correspondence with AFM topography (inset, Fig. 3j). Furthermore, cross-sectional AC-STEM at the phase boundary directly visualizes the abrupt α/β′ transition and reveals a grain boundary that pins the wrinkle propagation front. This confinement creates in-plane heterophase junctions between α and β′ domains.

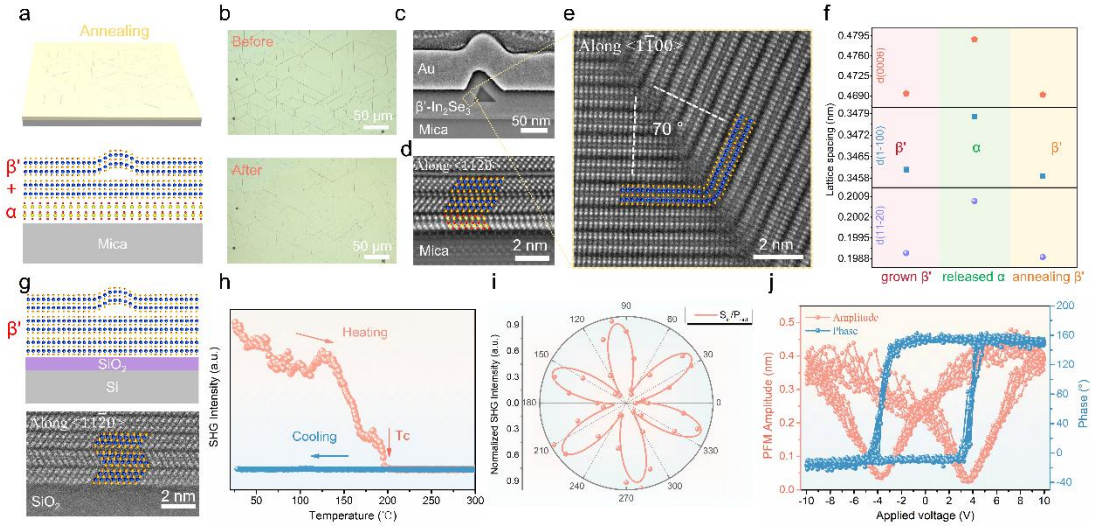


**Figure 4| Annealing-mediated strain relaxation triggers reversible β′ → α → β′ phase transformation in $In_2Se_3$. a** Schematic illustration depicting wrinkle relaxation via annealing, leading to formation of monolayer α-phase and multilayer β′-$In_2Se_3$ films. **b** Optical images of strain-released α-$In_2Se_3$ films on mica before and after annealing. **c** Cross-sectional HAADF image of the wrinkle after annealing. **d** Cross-sectional HAADF image of the annealed multilayer α-$In_2Se_3$/mica interface along the <11$\bar{2}$0> zone axis **e** Atomic HAADF image of the

maximum bending angle region (dashed box in Fig.4 **c**). **f** Evolution of interplanar spacing during the phase transition from as-grown β′-$In_2Se_3$ on mica to strain-released α-$In_2Se_3$ and subsequent annealing-mediated β′ reversion. **g** Schematic and AC-STEM characterization of phase-pure β′-$In_2Se_3$ via annealing strain-released α-$In_2Se_3$ transferred onto rigid $SiO_2$/Si substrates. **h** Temperature-dependent SHG response of strain-released α-$In_2Se_3$. **i** Angle-resolved SHG spectra of strain-released α-$In_2Se_3$ films on mica before annealing. **j** PFM tests of α-$In_2Se_3$ transferred on Au-coated $SiO_2$/Si substrate before annealing.

It is also found that thermal annealing could effectively eliminate wrinkles and improves film morphology, thereby triggering the reversion of the α-phase back to the β′-phase. As depicted in Fig. 4a, the α-$In_2Se_3$ film (formed via strain release from β′-$In_2Se_3$ on mica) was annealed at 350 °C under $N_2$ for 15 minutes, followed by natural cooling. Fig. 4b reveals a clear morphological contrast before and after annealing. Cross-sectional HAADF image of the film after annealing (Fig. 4c) demonstrates that the annealed $In_2Se_3$ film regains intimate contact with the mica substrate. AC-STEM image of the $In_2Se_3$/mica interface confirms that annealing re-establishes a vertical heterophase junction comprising monolayer α-$In_2Se_3$ and multilayer β'-$In_2Se_3$ on the mica. Atomic-resolution image (Fig. 4e) at the region of maximum bending angle (dashed box in Fig. 4c), reveals that the wrinkle remains persistently aligned along the $<1\bar{1}00>$ direction. Notably, within the QLs structure of the reformed β'-$In_2Se_3$, the central Se atom occupies the symmetric position, indicating the absence of out-of-plane ferroelectricity. Even at bending angles up to 70°, the atomic arrangement within the QLs remains consistent on both sides of the kink. This structural rigidity contrasts with the α-phase, which forms oppositely polarized domains across similar kinks.

We further employed XRD to probe the evolution in the in-plane $(11\bar{2}0)$ and $(1\bar{1}00)$, as well as the out-of-plane (0006) interplanar spacings before and after annealing (Supplementary Fig. 21-23). Fig. 4f summarizes the extracted lattice spacings corresponding to three distinct states: the initially grown β′- $In_2Se_3$ film on mica, the α-$In_2Se_3$ film formed by direct strain release and β′-$In_2Se_3$ transition on mica by subsequent annealing. The change of lattice spacing further confirm the annealing-induced reversion from strain-released α-$In_2Se_3$ back to the β′-phase. Furthermore, the

re-established intimate contact with mica substrate after annealing imposes compressive strain. As evidenced by the substantially reduced interplanar spacings in the annealed β′-$In_2Se_3$ compared to the strain-released α-$In_2Se_3$ (Fig. 4f).

Earlier analysis attributed the formation of monolayer α-$In_2Se_3$/multilayer β′-$In_2Se_3$ heterostructures under slow cooling exclusively to strain dissipation into the flexible mica substrate. To further validate this conclusion, strain-released α-$In_2Se_3$ was transferred onto rigid $SiO_2$/Si and annealed under identical conditions. Cross-sectional atomic schematics and HAADF images (Fig. 4g) reveal that the $In_2Se_3$ layer in direct contact with the $SiO_2$ substrate retains the β′-phase (Supplementary Fig. 24). This retention is attributed to the inability of the interfacial β′-$In_2Se_3$ to dissipate strain into the rigid substrate during cooling. Furthermore, we investigated the temperature-dependent second-harmonic generation (SHG) response of stress-released α-$In_2Se_3$. As shown in Fig. 4h, the SHG signal disappears above 200 °C and does not recover upon cooling, indicating an irreversible phase transition. Polarization-dependent SHG before heating confirmed out-of-plane (OOP) inversion symmetry breaking (six-fold pattern), which disappeared after annealing (Supplementary Fig. 25). Finally, piezoresponse force microscopy (PFM) on strain-released α-$In_2Se_3$ transferred onto Au/$SiO_2$/Si revealed clear OOP ferroelectricity (phase hysteresis and amplitude butterfly loops). Significantly, these ferroelectric signatures vanished post-annealing (Supplementary Fig. 26), confirming the transformation to a centrosymmetric structure and the loss of OOP ferroelectricity.

**Device performance**

To investigate the electrical properties, we fabricated back-gated field-effect transistors (FETs) using phase-engineered $In_2Se_3$ films. Fig. 5a schematically illustrates ferroelectric FET (FeFET) based on strain-released α-$In_2Se_3$. Corresponding cross-sectional HAADF-STEM imaging and EDS elemental mapping (Fig. 5b) confirm a α-$In_2Se_3$ channel capped by a 15 nm $Al_2O_3$ passivation layer. As a ferroelectric semiconductor, α-$In_2Se_3$ uniquely hosts both n-type mobile charges and polarization-bound charges, enabling non-volatile resistance switching controlled by Vgs. In the polarization-down (P-down) state (Fig. 5c), positive bound charges accumulate at α-

$In_2Se_3/SiO_2$ interface, inducing pronounced band bending, thereby accumulating mobile electrons and establishing a low-resistance state (LRS, "On state"). Conversely, under polarization-up (P-up) conditions, the reversed built-in field and attendant band bending deplete electrons at the α-$In_2Se_3/SiO_2$ interface, driving the device into a high-resistance state (HRS, "Off state"). This gate-controlled switching between polarization orientations manifests as pronounced hysteresis in transfer characteristics.

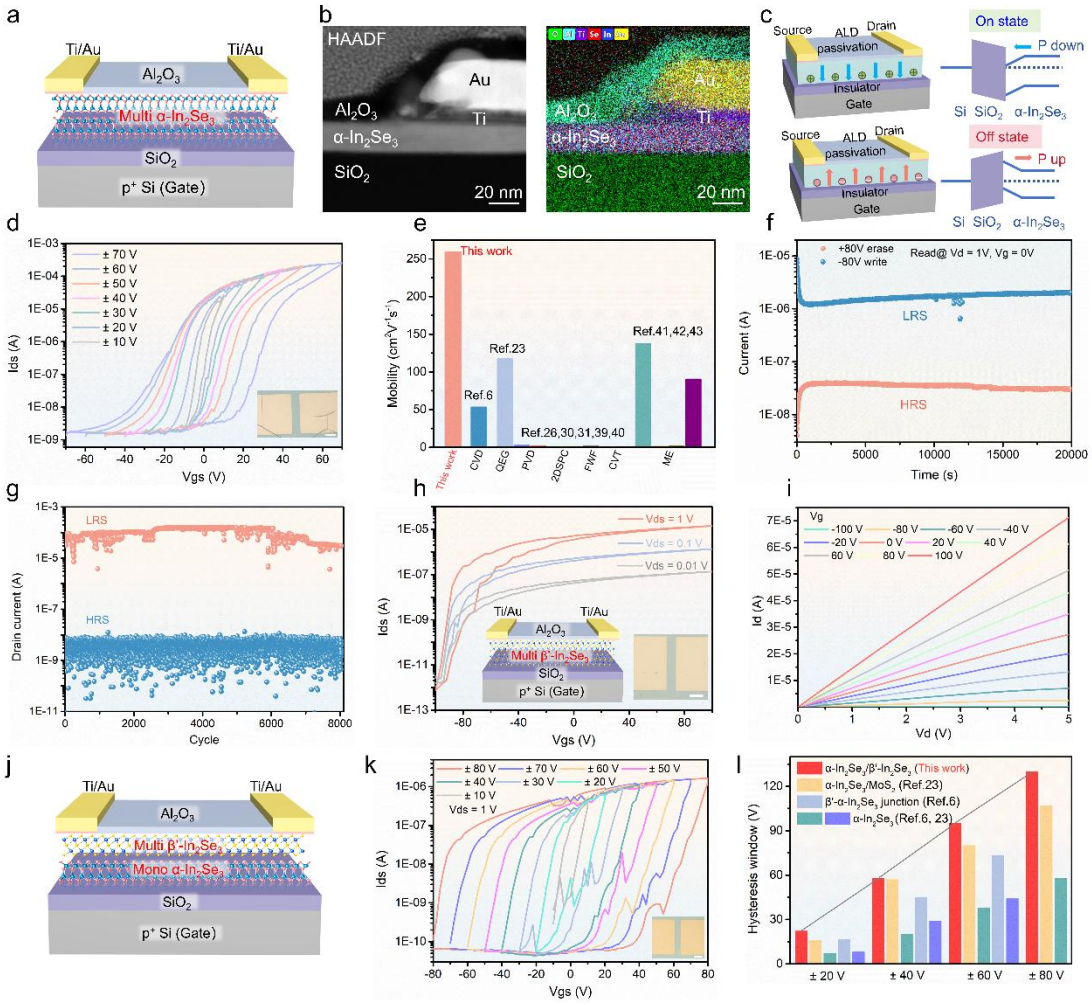


**Figure 5| Mechanisms and performance of phase-engineered $In_2Se_3$ field-effect transistors.** **a** Schematic of the α-$In_2Se_3$-based ferroelectric field-effect transistors (Fe-FETs). **b** HAADF images and corresponding EDS mapping of the cross-sectional α-$In_2Se_3$ Fe-FETs. **c** Operational states and band diagrams of α-$In_2Se_3$ Fe-FETs under P-down and P-up conditions. **d** Hysteresis transfer curve in α-$In_2Se_3$ Fe-FETs (Vds = 1 V). Inset: Optical image of α-$In_2Se_3$ Fe-FETs. Scale bar: 10 μm. **e** Comparative μ-FET analysis of α-$In_2Se_3$ prepared by alternative methods: CVD[6], QEG[23], PVD[26,39], 2DSPC[30], FWF[31], CVT[40] and ME[41-43]. **f** Polarization retention

characterization in α-$In_2Se_3$ Fe-FETs (±80 V write/erase, read at Vgs=0V and Vds=1V). **g** Endurance of the α-$In_2Se_3$ Fe-FETs device after 8000 write/erase cycles. **h** Transfer characteristics of β′-$In_2Se_3$ FETs at varying Vds. Inset: Schematic diagram and optical image of the device. Scale bar: 10 μm. **i** Output characteristics of β′-$In_2Se_3$ FETs. **j** Schematic of Fe-FETs based on vertical α-$In_2Se_3$/β′-$In_2Se_3$ heterophase junction. **k** Hysteresis transfer curve in α-$In_2Se_3$/β′-$In_2Se_3$ Fe-FETs. **l** Hysteresis window comparison of our α-$In_2Se_3$/β′-$In_2Se_3$ vertical heterophase junction, α-$In_2Se_3$/$MoS_2$ heterostructure[23], α-$In_2Se_3$,[6,23] and α-$In_2Se_3$/β′-$In_2Se_3$ lateral heterophase junction[6] devices within various voltage sweep ranges.

Fig. 5d shows substantial hysteresis loops under bidirectional Vgs sweeps. At ± 60 V sweep range, a hysteresis window of ≈37 V is achieved with an on/off ratio >$10^5$. Compared to other α-$In_2Se_3$ flakes prepared by alternative strategies[6,23,26,39-44] (Fig. 5e), our device exhibits a high mobility of 259 $cm^2$ $V^{-1}$ $s^{-1}$ in reverse scan—more than double the value reported recently for QEG-α-$In_2Se_3$. Furthermore, benefiting from phase-pure α-$In_2Se_3$ and ALD passivation, the devices demonstrate excellent reliability, with long retention (>20,000 s) under ±80 V write/erase pulses (Figs. 5f) and high endurance (>8,000 cycles) (Fig. 5g). For comparison, we fabricated back-gated FETs using β′-$In_2Se_3$ films (dual-sweep transfer characteristics shown in Fig. 5h). Unlike the non-centrosymmetric, ferroelectric α-phase, β′-$In_2Se_3$ FETs show minimal hysteresis, with only an 8 V memory window under ±90 V gate sweeps (Vds = 0.1 V). Nevertheless, the high on/off ratio ($10^7$ at Vds = 1 V) and linear output characteristics (Fig. 5i) confirm excellent material quality and contact properties.

We also fabricated FeFETs based on directly grown vertical heterophase structures comprising a monolayer α-$In_2Se_3$ and multilayer β′-$In_2Se_3$ (Fig. 5j). Leveraging the reported ~2.8 eV bandgap of monolayer α-$In_2Se_3$, we incorporated the ferroelectric monolayer as gate dielectric component to regulate electronic properties of the n-type β′-$In_2Se_3$ channel[23,45]. As shown in Supplementary Fig. 27, when α-$In_2Se_3$ is in the P-up polarization state, a trap layer forms at the α-$In_2Se_3$/β′-$In_2Se_3$ interface, confining electrons and depleting the β′-$In_2Se_3$ channel, thereby switching the device to the off-state[23,46]. Conversely, under P-down polarization, holes become confined at the interface while electrons accumulate in β′-$In_2Se_3$, establishing the on-state. Fig. 5h

exhibits clockwise hysteresis in transfer characteristics under varying gate voltages, achieving 136 V memory window within ±80 V sweep range. Notably, compared to recently reported transferred α-$In_2Se_3$/$MoS_2$ vertical heterostructure FETs (Fig. 5l), our single-step grown α-$In_2Se_3$/β′-$In_2Se_3$ vertical heterophase junctions exhibit larger hysteresis windows and higher on/off ratios[23], demonstrating superior memory performance[47].

## Conclusion

In summary, we find that growth of $In_2Se_3$ on mica substrates under different conditions yields only the β' phase or monolayer α phase/multilayer β' phase. The direct growth of phase-pure α-$In_2Se_3$ on mica substrates is constrained, and this limitation originates from substrate-induced compressive epitaxial strain and mechanical flexibility. Crucially, we achieved pure α-phase formation by directly releasing strain in β′-$In_2Se_3$ films on mica, providing a rapid and effective method for preparing large-area α-$In_2Se_3$ films. Transistors fabricated from α-$In_2Se_3$, β′-$In_2Se_3$, and vertical monolayer α/β′ $In_2Se_3$ heterophase structures exhibit high electron mobility, high on/off ratio and large hysteresis window, establishing a foundation for phase-controlled 2D material growth and next-generation electronic devices.

## Methods

### CVD/PVD growth of large-area α-$In_2Se_3$ films

α-$In_2Se_3$ films were synthesized on the F-mica ($KMg_3AlSi_3O_{10}F_2$) substrates using a 2-inch tube furnace. For rapid/slow-cooling CVD growth, Se and $In_2O_3$ precursors were positioned in two separate temperature zones, with the Se source located 15 cm upstream of the $In_2O_3$ source. the zones were heated to 280 °C and 700 °C, respectively. Growth proceeded for 18 minutes under a carrier gas flow of mixed Ar/$H_2$. Post-growth cooling to room temperature was performed at rates of ~20 °C/min and 1 °C/min, respectively. For salt-assisted CVD, $In_2O_3$ and KI were thoroughly mixed at a mass ratio of 60:1. The mixture and Se were positioned in two separate temperature zones heated to 280 °C and 620 °C, respectively, all other conditions remained identical. After

growth, the sample underwent natural cooling to room temperature. For rapid/slow-cooling PVD growth, mica substrate and α-$In_2Se_3$ powder source were co-located within a single temperature zone. Deposition was conducted at 850 °C for 18 minutes under Ar carrier gas flow. Post-deposition cooling to room temperature was implemented at rates of 21 °C/min and 1 °C/min, respectively. For salt-assisted PVD, α-$In_2Se_3$ powder and KI were thoroughly mixed at a mass ratio of 60:1 and deposition occurred at 750 °C, with all other conditions identical. After deposition, the system was allowed to cool naturally to room temperature.

**Transfer method of α-$In_2Se_3$ films**

The α-$In_2Se_3$ film grown on mica was transferred onto specific target substrates using a poly (methyl methacrylate) (PMMA)-mediated method. PMMA solution was spin-coated onto the α-$In_2Se_3$/mica at 1500 rpm for 1 min, followed by baking at 120 °C for 3 min. The PMMA film supporting the α-$In_2Se_3$ layer was then delaminated from the mica substrate using deionized water and subsequently transferred onto the target substrate or TEM grid. Finally, the PMMA was removed by dissolving it in acetone twice.

**Materials characterization**

The morphology of α-$In_2Se_3$ films were characterized by optical microscope (Leica, DM1750M), AFM (Bruker, Dimension ICON), Raman and PL spectroscopy (LabRAM Evolution, Horiba scientific), In-plane XRD (Rigaku, SmartLab), temperature dependent XRD (ARL Equinox 3500), plan view TEM (FEI Talos F200X), PFM (MFP 3D, Oxford). SHG mapping were measured in the reflection mode via a modified confocal micro-Raman spectrometer (HR800, Horiba/Jobin Yvon) and picosecond pulsed laser at 1064 nm was applied for SHG measurements. The cross-sectional TEM samples were prepared by a dual-beam FIB scanning electron microscopy system (FEI Helios G4 UX). Microstructural analyses of interface were performed using AC-STEM (FEI, Themis Z).

**Device fabrication and characterization**

α-$In_2Se_3$, β′-$In_2Se_3$ and α/β′-$In_2Se_3$ films were transferred onto $SiO_2$ (285 nm)/Si substrate. Laser direct writing lithography and e-beam evaporation of Ti/Au (5 nm/50

nm) were used to fabricate back-gate FETs. All devices are deposited with 15 nm-thick $Al_2O_3$ passivation by ALD to avoid oxygen/moisture and to enhance device stability and performance. All FETs were tested by Keithley 4200 semiconductor analyzer in a probe station. The field-effect mobility (μ) was extracted from the equation $\mu = \frac{dI_{ds}}{dV_{gs}} \times \frac{L}{WC_iV_{ds}}$, where $\frac{dI_{ds}}{dV_{gs}}$ is the maximum transconductance; $L$ and $W$ are the channel length and width, respectively; $C_i$ is the capacitance of the $SiO_2$ ($1.15 \times 10^{-4}$ F $m^{-2}$); Vds is the drain voltage.

**Acknowledgement**

We acknowledge the support from the National Natural Science Foundation of China (Grant Nos. 52202179, 62174169, 52372118 & 62201345).

**Author contributions**

T.W., L.X. and X.Z. conceived and designed the experiments. L.X., T.W. and X.Z. performed the growth. L.X., T.W. conducted strain-released experiments. Q.R., L.S, L.X. and X.Z. performed XRD measurements and analysis. D.L. performed FIB for TEM tests. Y.Y., Y.H., M.W. and L.X. performed SHG tests. X.F., L.X., T.T., H.G., Z.W. and Y.M. performed device fabrication and analysis. Y.W. and Z.S. carried out the CVD equipment renovation.

**Competing interests**

The authors declare no conflict of interest.

**References**

1 Kim, K. H. *et al.* Scalable CMOS back-end-of-line-compatible AlScN/two-dimensional channel ferroelectric field-effect transistors. *Nat. Nanotechnol.* **18**, 1044-+ (2023).
2 Zheng, C. *et al.* Room temperature in-plane ferroelectricity in van der Waals $In_2Se_3$. *Sci. Adv.* **4** (2018).
3 Xu, C. *et al.* Two-Dimensional Antiferroelectricity in Nanostripe-Ordered $In_2Se_3$. *Phys. Rev. Lett.* **125** (2020).
4 Xu, C. *et al.* Two-dimensional ferroelasticity in van der Waals β'-$In_2Se_3$. *Nat. Commun.* **12**, 3665 (2021).
5 Sharma, P. *et al.* A room-temperature ferroelectric semimetal. *Sci. Adv.* **5** (2019).
6 Han, W. *et al.* Phase-controllable large-area two-dimensional $In_2Se_3$ and ferroelectric heterophase junction. *Nat. Nanotechnol.* **18**, 55-63 (2023).

7 Xu, L. *et al.* Pseudosymmetric Epitaxy for Scalable Growth of Uniform Two-Dimensional Ferroelectric α-$In_2Se_3$ Monolayer. *Nano Lett.* **25**, 8423-8430 (2025).
8 Wang, S. *et al.* Two-dimensional ferroelectric channel transistors integrating ultra-fast memory and neural computing. *Nat. Commun.* **12** (2021).
9 Claro, M. S. *et al.* Wafer-Scale Fabrication of 2D β-$In_2Se_3$ Photodetectors. *Adv. Opt. Mater.* **9** (2021).
10 Lv, B. H. *et al.* Layer-dependent ferroelectricity in 2H-stacked few-layer α-$In_2Se_3$. *Mater. Horiz.* **8**, 1472-1480 (2021).
11 He, Q. M. *et al.* Epitaxial Growth of Large Area Two-Dimensional Ferroelectric α-$In_2Se_3$. *Nano Lett.* **23**, 3098-3105 (2023).
12 Xiao, J. *et al.* Intrinsic Two-Dimensional Ferroelectricity with Dipole Locking. *Phys. Rev. Lett.* **120**, 227601 (2018).
13 Zhou, Y. *et al.* Out-of-Plane Piezoelectricity and Ferroelectricity in Layered α-$In_2Se_3$ Nanoflakes. *Nano Lett.* **17**, 5508-5513 (2017).
14 Zhou, S. Y. *et al.* Periodic Ferroelectric Stripe Domains in α-$In_2Se_3$ Nanoflakes Grown via Reverse-Flow Chemical Vapor Deposition. *ACS Appl. Mater. Interfaces* **15**, 23613-23622 (2023).
15 Io, W. F. *et al.* Temperature- and thickness-dependence of robust out-of-plane ferroelectricity in CVD grown ultrathin van der Waals α-$In_2Se_3$ layers. *Nano Res.* **13**, 1897-1902 (2020).
16 Cui, C. J. *et al.* Intercorrelated In-Plane and Out-of-Plane Ferroelectricity in Ultrathin Two-Dimensional Layered Semiconductor $In_2Se_3$. *Nano Lett.* **18**, 1253-1258 (2018).
17 Zheng, X. D. *et al.* Phase and polarization modulation in two-dimensional $In_2Se_3$ via in situ transmission electron microscopy. *Sci. Adv.* **8**, 0773 (2022).
18 Lin, M. *et al.* Controlled Growth of Atomically Thin $In_2Se_3$ Flakes by van der Waals Epitaxy. *J. Am. Chem. Soc.* **135**, 13274-13277 (2013).
19 Rashid, R. *et al.* Shape-control growth of 2D-$In_2Se_3$ with out-of-plane ferroelectricity by chemical vapor deposition. *Nanoscale* **12**, 20189-20201 (2020).
20 Yang, K. M. *et al.* Controllable growth α-$In_2Se_3$ flakes by chemical vapor deposition. *Results Phys.* **51** (2023).
21 Dai, M. J. *et al.* Intrinsic Dipole Coupling in 2D van der Waals Ferroelectrics for Gate-Controlled Switchable Rectifier. *Adv. Electron. Mater.* **6** (2020).
22 Wan, S. *et al.* Nonvolatile Ferroelectric Memory with Lateral β/α/β $In_2Se_3$ Heterojunctions. *ACS Appl. Mater. Interfaces* **14**, 25693-25700 (2022).
23 Si, K. *et al.* Quasi-equilibrium growth of inch-scale single-crystal monolayer alpha-$In_2Se_3$ on fluor-phlogopite. *Nat. Commun.* **15**, 7471 (2024).
24 Feng, W. *et al.* Sensitive Electronic-Skin Strain Sensor Array Based on the Patterned Two-Dimensional α-$In_2Se_3$. *Chem. Mater.* **28**, 4278-4283 (2016).
25 Poh, S. M. *et al.* Molecular-Beam Epitaxy of Two-Dimensional $In_2Se_3$ and Its Giant Electroresistance Switching in Ferroresistive Memory Junction. *Nano Lett.* **18**, 6340-6346 (2018).
26 Zhang, W. *et al.* a-$In_2Se_3$ Nanostructure-Based Photodetectors for Tunable and Broadband Response. *ACS Appl. Nano Mater.* **6**, 8795-8803 (2023).

27 Lyu, F. J. *et al.* Temperature-Driven α-β Phase Transformation and Enhanced Electronic Property of 2H α-$In_2Se_3$. *ACS Appl. Mater. Interfaces* **14**, 23637-23644 (2022).
28 Si, M. W. *et al.* A ferroelectric semiconductor field-effect transistor. *Nat. Electron.* **2**, 580-586 (2019).
29 Liu, B. T. *et al.* Phase Tailoring of $In_2Se_3$ Toward van der Waals Vertical Heterostructures via Selenization of γ-InSe Semiconductor. *Small Methods* (2024).
30 Hsu, C. P. *et al.* Synthesis and Phase Transition of Large-Area Layered Ferroelectric Semiconductor α-$In_2Se_3$ via 2D Solid-Phase Crystallization. *Adv. Electron. Mater.* **10** (2024).
31 Shin, J. *et al.* $In_2Se_3$ Synthesized by the FWF Method for Neuromorphic Computing. *Adv. Electron. Mater.* **11** (2025).
32 Zhang, Z. M. *et al.* Atomic Visualization and Switching of Ferroelectric Order in β-$In_2Se_3$ Films at the Single Layer Limit. *Adv. Mater.* **34** (2022).
33 Vanlanduyt, J. *et al.* PHASE-TRANSITIONS IN $IN_2SE_3$ AS STUDIED BY ELECTRON-MICROSCOPY AND ELECTRON-DIFFRACTION. *Physica Status Solidi a-Applied Research* **30**, 299-314 (1975).
34 Wang, L. *et al.* In-Plane Ferrielectric Order in van der Waals β'-$In_2Se_3$. *ACS Nano* **18**, 809-818 (2023).
35 Zheng, D. Q. *et al.* Ultrathin two-dimensional van der Waals asymmetric ferroelectric semiconductor junctions. *J. Appl. Phys.* **132**, 054101 (2022).
36 Wang, N. *et al.* Is all epitaxy on mica van der Waals epitaxy? *Mater. Today Nano* **20** (2022).
37 Lu, L. *et al.* Atomic Scale Understanding of the Epitaxy of Perovskite Oxides on Flexible Mica Substrate. *Adv. Mater. Interfaces* **7** (2020).
38 Han, E. *et al.* Bend-Induced Ferroelectric Domain Walls in α-$In_2Se_3$. *ACS Nano* **17**, 7881-7888 (2023).
39 Zhou, J. *et al.* Controlled Synthesis of High-Quality Mono layered α-$In_2Se_3$ via Physical Vapor Deposition. *Nano Lett.* **15**, 6400-6405 (2015).
40 Anandan, M. *et al.* High-responsivity broad-band sensing and photoconduction mechanism in direct-Gap α-$In_2Se_3$ nanosheet photodetectors. *Nanotechnology* **31** (2020).
41 Wang, L. *et al.* Exploring Ferroelectric Switching in α-$In_2Se_3$ for Neuromorphic Computing. *Adv. Funct. Mater.* **30**, 2004609 (2020).
42 Wang, S. Y. *et al.* Strong Anisotropic Two-Dimensional $In_2Se_3$ for Light Intensity and Polarization Dual-Mode High-Performance Detection. *ACS Appl. Mater. Interfaces* **15**, 3357-3364 (2023).
43 Li, X. *et al.* Multi-Functional Platform for In-Memory Computing And Sensing Based on 2D Ferroelectric Semiconductor α-$In_2Se_3$. *Adv. Funct. Mater.* **34** (2024).
44 Feng, W. *et al.* Phase-Engineering-Driven Enhanced Electronic and Optoelectronic Performance of Multilayer $In_2Se_3$ Nanosheets. *ACS Appl. Mater. Interfaces* **10**, 27584-27588 (2018).
45 Lyu, F. J. *et al.* Thickness-dependent band gap of α-$In_2Se_3$ from electron energy loss spectroscopy to density functional theory calculations. *Nanotechnology* **31**

(2020).
46 Chen, J. *et al.* Polarized Tunneling Transistor for Ultrafast Memory. *ACS Nano* **17**, 12374-12382 (2023).
47 Hong, A. J. *et al.* Graphene Flash Memory. *ACS Nano* **5**, 7812-7817 (2011).

# Supplementary Files

This is a list of supplementary files associated with this preprint. Click to download.

- Supplementarymaterials.docx
- Vedio1CVDtriangulardomain.mp4
- Vedio2CVDfilms.mp4
- Vedio3PVDtriangulardomain.mp4
- Vedio4PVDfilms.mp4
- Vedio5Domaindisapear.mp4